A&A 419, 991–998 (2004)
DOI: 10.1051/0004-6361:20035757

Astronomy
&
Astrophysics

Time-dependent ejection velocity model for the outflow of Hen 3-1475*

P. F. Velázquez[1], A. Riera[2,3], and A. C. Raga[1]

[1] Instituto de Ciencias Nucleares, UNAM, Ciudad Universitaria, Apdo. Postal 70-543, CP 04510, Mexico D.F., Mexico
e-mail: `raga@nuclecu.unam.mx`
[2] Departament de Física i Enginyeria Nuclear, Universitat Politècnica de Catalunya, Escola Universitària Politècnica de Vilanova i La Geltrú, Av. Víctor Balaguer s/n, 08800 Vilanova i la Geltrú, Spain
e-mail: `angels.riera@upc.es`
[3] Departament d'Astronomia i Meteorologia, Universitat de Barcelona, Av. Diagonal 647, 08028 Barcelona, Spain

Received 28 November 2003 / Accepted 25 February 2004

Abstract. We present 2D axisymmetric and 3D numerical simulations of the proto-planetary nebula Hen 3-1475, which is characterized by a remarkably highly collimated optical jet, formed by a string of shock-excited knots along the axis of the nebula. It has recently been suggested that the kinematical and morphological properties of the Hen 3-1475 jet could be the result of an ejection variability of the central source (Riera et al. 2003). The observations suggest a periodic variability of the ejection velocity superimposed on a smoothly increasing ejection velocity ramp. From our numerical simulations, we have obtained intensity maps (for different optical emission lines) and position-velocity diagrams, in order to make a direct comparison with the HST observations of this object. Our numerical study allows us to conclude that a model of a precessing jet with a time-dependent ejection velocity, which is propagating into an ISM previously perturbed by an AGB wind, can succesfully explain both the morphological and the kinematical characteristics of this proto-planetary nebula.

Key words. ISM: jets and outflows – planetary nebulae: individual: Hen 3-1475 – methods: numerical – hydrodynamics

1. Introduction

Recent images of young PNe obtained with the HST have revealed that almost all of them have aspherical morphologies. Also, a significant fraction show bipolar or multipolar lobes, highly collimated outflows or jets and other complex structures such as loops (see, e.g., Sahai & Trauger 1998; García-Lario et al. 1999; Trammell & Goodrich 2002). Sahai & Trauger (1998) suggested that the outflows (i.e., collimated fast winds, hereafter CFWs) acting during the early post-AGB phase may have an important impact in the formation of these complex structures. However, the mechanism(s) producing the collimated fast winds or jets are not well understood.

The most promising scenarios for producing CFWs or jets are:

- (i) magnetized accretion disk and binary stellar system (see, e.g., Soker & Livio 1994; Blackman et al. 2001);
- (ii) a rapidly rotating star with a toroidal magnetic field (see, e.g., García-Segura et al. 1999; García-Segura & López 2000).

Recently, the interaction of CFWs and the AGB envelope has been explored both analytically and numerically (Soker & Rappaport 2000; Lee & Sahai 2003; García-Arredondo & Frank 2003).

The proto-planetary nebula (PPN) Hen 3-1475 shows a very well collimated jet, formed by a string of knots distributed along the main axis of the nebula (reminiscent of a HH object). Hen 3-1475 has been the object of optical imaging from the ground (Riera et al. 1995) and with the Hubble Space Telescope (HST) (Bobrowsky et al. 1995; Borkowski et al. 1997; Ueta et al. 2000), near-infrared photometry (García-Lario et al. 1997; Rodrigues et al. 2003), optical polarization (Rodrigues et al. 2003), optical spectroscopy (Riera et al. 1995; Bobrowsky et al. 1995; Borkowski & Harrington 2001; Sánchez Contreras & Sahai 2001; Riera et al. 2002, 2003), and proper motion studies (Borkowski & Harrington 2001; Riera et al. 2002, 2003).

The central region is probably a dusty disk (or torus). The densest parts of the disk are seen in the WFPC2 images of Borkowski et al. (1997) as dark patches. The intrinsic polarization and large reddening of the circumstellar region of Hen 3-1475 has been studied in detail by Rodrigues et al. (2003). The presence of CO molecular emission suggests the existence of large amounts of neutral gas. The CO emission shows an expanding torus of material (Knapp et al. 1995; Bujarrabal et al. 2001). The recent CO observations of Huggins et al. (2004) show the presence of an expanding biconical

---

Send offprint requests to: P. F. Velázquez,
e-mail: `pablo@nuclecu.unam.mx`

* Based on observations made with the Hubble Space Telescope, obtained from the Data Archive at the Space Telescope Science Institute, which is operated by the Association of Universities for Research in Astronomy, Inc., under NASA contract NAS5-26555.

envelope, and provide strong evidence for entrainment of the molecular gas by the high-velocity jets. The OH emission suggests the existence of an aspherical shell expanding at 25 km s^{-1} (Bobrowsky et al. 1995; Zijlstra et al. 2001).

The radio continuum indicates the presence of a compact, ionized region surrounding the central B star (Bobrowsky et al. 1995; Knapp et al. 1995). Optical, ground based spectroscopy of the central source revelead the presence of P-Cygni Balmer line profiles (Riera et al. 1995), which indicates the presence of mass outflows at high velocities. An analysis of a STIS, long-slit Hα spectrum of the central region of Hen 3-1475 (Sánchez Contreras & Sahai 2001), suggests the presence of two different winds outflowing from the central star at high velocities. The highest velocity outflowing wind is highly collimated close to the central star, and shows a radially increasing velocity.

The emitting knots show extremely broad, double-peaked emission line profiles (with FWHM from 400 to 1000 km s^{-1}, Borkowski & Harrington 2001; Riera et al. 2003). The radial velocities observed along the Hen 3-1475 jet decrease with increasing distance to the central source, showing abrupt velocity changes in the transition regions from each (sub)condensation to the next one.

From a comparison of the spectra observed for the intermediate knots of Hen 3-1475 with the spectra predicted by plane-parallel shocks, Riera et al. (1995) concluded that the emission is produced in a shock wave which propagates through a nitrogen-enriched medium. Predictions from plane-parallel shock models (adopting type I PN abundances) with shock velocities from 100 → 150 km s^{-1} qualitatively reproduce the observed spectra (Riera et al. 2003).

Recently, *Chandra* has detected X-ray emission from Hen 3-1475 (Guerrero et al. 2004; Sahai et al. 2004). The X-ray source position coincides with the innermost optical knot NW1, and the X-ray emitting gas is probably shock heated. The X-ray spectrum implies a temperature of $\sim 2.4 \times 10^6$ K, and the observed X-ray luminosity implies a shock velocity ~400 km s^{-1} (Guerrero et al. 2004; Sahai et al. 2004).

Recently, it has been suggested that kinematic and morphological properties of the Hen 3-1475 jet could be the result of a variability of the central source (Riera et al. 2003). During the past 15 years, time-dependent ejection velocity models have been studied and applied to HH jets, and these models in principle can also be applied to the Hen 3-1475 jet. In these models, the chain of knots observed in the jet is assumed to correspond to the successive internal working surfaces[1] resulting from a (possibly periodic) ejection velocity variability. One-dimensional analytic (Raga et al. 1990; Cantó et al. 2000), as well as axisymmetric and 3-D numerical simulations (Völker et al. 1999; Raga et al. 2002; Masciadri et al. 2002) have been carried out for different functional forms for the ejection velocity variability.

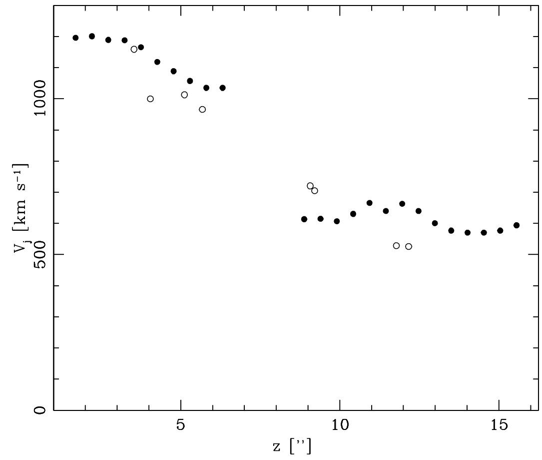

Fig. 1. Velocity of the emiting gas as a function of distance z from the source, reconstruted from the ground-based radial velocities (solid circles) and the STIS spectroscopy (open circles).

In the present paper, we investigate whether or not the properties of the jets of Hen 3-1475 can be the result of the variability of the ejection velocity. As far as we are aware, our work is the first attempt to obtain a gasdynamical simulation of this object. The origin of both the collimation mechanism and of the ejection velocity variability is not studied in this paper.

The present paper is organized as follows: in Sect. 2, a variable velocity ejection law is obtained for the case of Hen 3-1475; the initial conditions and assumptions for the 2-D and 3-D numerical simulations are presented in Sect. 3; in Sect. 4, we present the results of the temporal evolution from 2-D axisymmetric numerical simulation (Sect. 4.1) and the comparison of 3-D results with HST observations (Sect. 4.2); finally, in Sect. 5, we give our conclusions.

2. A variable velocity ejection law for Hen 3-1475

We now consider the ground-based and the STIS HST spectroscopy, together with proper motion measurements (taken from Riera et al. 2003) of the Hen 3-1475 jet. We first deproject the distance z from the source and the velocity $v(z)$ for an assumed angle $\phi = 50°$ between the outflow axis and the plane of the sky (Borkowski & Harrington 2001). In this way, we obtain the physical velocity of the emitting gas as a function of distance from the source (see Fig. 1).

From Fig. 1, we see that the flow velocity decreases in an approximately monotonic way as a function of increasing distances from the source. Such a velocity configuration suggests a time-dependent ejection velocity which smoothly increases as a function of time (with larger velocities at more recent times). Also, we need to superpose (on this "smooth ramp" variability) a variation in the ejection velocity with an appropriate period and amplitude in order to obtain internal working surfaces at positions that approximately correspond to the positions of the knots along the observed jet.

---

[1] A "working surface" is a double shock structure produced by the propagation of a fast flow into a slower flow. This working surface is formed by a bow shock sweeping up the material of the slow flow, an inward shock or Mach disk that decelerates the fast flow gas, and a contact discontinuity between them, separating the shocked slow and fast flow gas.

After trying a number of different functional forms for the ejection velocity variability, we have chosen the form:

$$v_{\rm j} = v_0 + v_1 \, \sin\left(2\,\pi(t - t_0)\,/\,\tau\right) + a\,t, \qquad (1)$$

which includes a periodic term (described by a sinusoidal function characterized by an amplitude velocity v_1 and a period τ), superimposed on a linear increase of the velocity (at a rate a). In Eq. (1), $t_0\,(<0)$ is the time at which the source is initially turned on ($t = 0$ corresponding to the time at which the observations were obtained). Through the computation of several models with different parameters, we find that the following parameter set: $v_0 = 400$ km s^{-1} (mean velocity), $v_1 = 150$ km s^{-1} (velocity variability half-amplitude), $\tau = 120$ yr (period of the sinusoidal veriability), $a = 1$ km s^{-1} yr^{-1} (slope of linear ramp) and $t_0 = -640$ yr (time at which the jet is turned on) produces jets with knot structures and kinematical properties similar to the ones of the Hen 3-1475 jet. We then use the ejection velocity variability given by Eq. (1) with this particular set of parameters in order to compute the axisymmetric and 3D jet simulations discussed in the following sections.

3. Numerical simulations

3.1. 2-D numerical simulation

The 2-D numerical simulations have been carried out with the axisymmetric version of the Yguazú–a code (which is described in detail by Raga et al. 2000). This code integrates the cylindrical gasdynamic equations (employing the "flux vector splitting" scheme of van Leer 1982) together with a system of rate equations for atomic/ionic species. With these rate equations, a non-equilibrium cooling function is computed. The reaction and cooling rates are described in detail by Raga et al. (2002). We have used the mean type I PN abundances from Kingsburgh & Barlow (1994).

The axisymmetric numerical simulations were computed on a 4-level binary adaptive grid, with a maximum resolution of 1.172×10^{15} cm along both axes. The computational domain is of $(12.0,\ 1.5) \times 10^{17}$ cm, along the axial (z) and radial (r) axes, respectively.

The jet is injected at $z = 0$ with the time-dependent ejection velocity given by Eq. (1) (and with the paremeter set given in Sect. 2). The jet has an initial radius $r_{\rm j} = 6 \times 10^{15}$ cm, (time-independent) density of 500 cm^{-3} (similar to the density derived by Riera et al. in preparation) and temperature $T_{\rm j} = 1000$ K.

We have carried out 2-D numerical simulations with two density distributions for the surrounding medium. First, we have assumed that the surrounding environment is homogeneous, with a density $n_{\rm env} = 10$ cm^{-3} and temperature $T_{\rm env} = 100$ K.

However, the high-velocity outflows of Hen 3-1475 are moving through the slow wind previously ejected by the star as a red giant on the AGB. The circumstellar envelope of Hen 3-1475 is far from being spherical as shown from the optical polarization maps and the spatial distribution of the CO and OH emission (see, e.g., Bobrowsky et al. 1995; Zijlstra et al. 2001; Bujarrabal et al. 2001; Rodrigues et al. 2003; Huggins et al. 2004). In order to include this, we have computed a second model, in which the outflow is moving into an AGB wind. For this model, we have assumed that the AGB remnant has an aspherical density distribution with high densities on the equator and lower densities on the poles, which is described by the following equation (taken from Mellema 1995),

$$\rho(R) = \rho_0 \left[1 - \alpha \left(\frac{1 - \exp(-2\beta \sin^2 \theta)}{1 - \exp(-2\beta)} \right) \right] (R_0/R)^2 \qquad (2)$$

where $R = \sqrt{r^2 + z^2}$ and θ is the angle with respect to r-axis. The parameter α determines the ratio between the density at the equator and at the pole, and β determines the way the density varies from the equator to the pole (see Mellema 1995). The value of ρ_0 is calculated from the mass loss rate as: $\rho_0 = \dot{M}/4\,\pi\,R_0^2\,v_{\rm env}$, where $v_{\rm env}$ is the expansion velocity of the AGB remnant. We have chosen $R_0 = r_{\rm j}$, a mass loss rate of $10^{-6}\,M_\odot$ yr^{-1} and an expansion velocity of 20 km s^{-1}. For α and β we adopt values of 0.7 and 3.0, respectively. With these parameters and Eq. (2) the range of the AGB wind density along z-axis is $\sim$[500, 0.05] cm^{-3} from the injection point to the z boundary, respectively.

3.2. 3-D numerical simulation

Axisymmetric numerical simulations are powerful tools for finding a time-dependent ejection velocity (such as the one given by Eq. (1)) which produces knots with appropriate positions and kinematical properties. However, the Hen 3-1475 jet has a "S"-like morphology, which is far from axisymmetric. Then, in order to reproduce this "S"-like shape, we have carried out 3-D numerical simulations, including a precession of the outflow axis with a period of 1500 yr and a half aperture angle for the precession cone of 7.5°. This precession produces approximately one half "wave" of the approximately helical jet beam within the observed length of the jet in Hen 3-1475 (in agreement with the observed images).

We then carry out a 3-D numerical simulation of a jet with the ejection velocity variability given in Sect. 2, and the precession described above. The numerical simulations were carried out with the 3-D version of Yguazú–a code, employing a five-level binary adaptive grid with a maximum resolution of 2.34×10^{15} cm. The computational domain was of $(3,\ 3,\ 12) \times 10^{17}$ cm along x-, y- and z-axis, respectively.

The outflow is injected at $x = y = 1.5 \times 10^{17}$ cm, on the $z = 0$ plane. The initial jet radius is 1.5×10^{16} cm, the initial number density is $n_{\rm j} = 500$ cm^{-3} and the temperature is $T_{\rm j} = 1000$ K. We have adopted a larger initial jet radius than in the axisymmetric simulations (see Sect. 3.1) in order to resolve the jet beam with $\sim$10 grid points (in the lower resolution, 3-D simulation).

In the 3-D simulation, we assume that the jet is moving into the AGB wind, for which we adopt the aspherical density function and parameters described in Sect. 3.1.

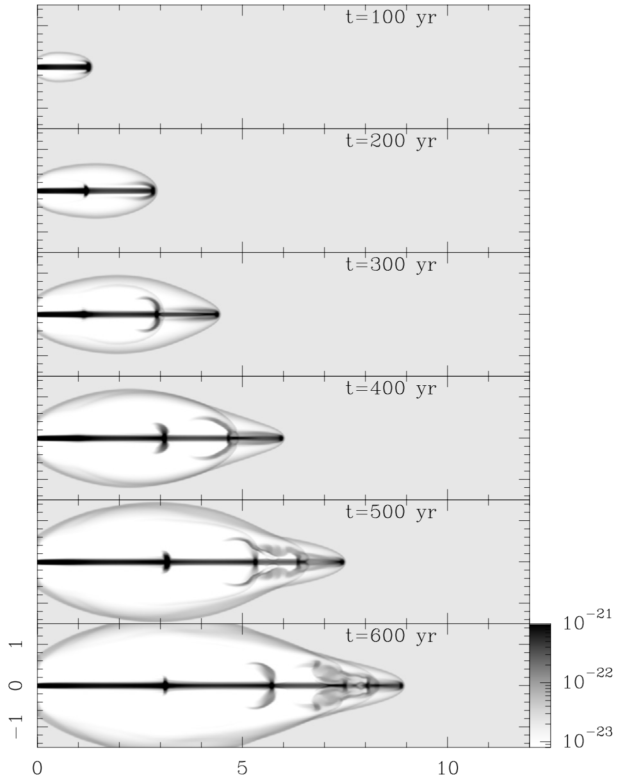

Fig. 2. Time evolution of the density stratification for the case of an outflow moving into a homogeneous environment. Integration times range from 100 to 600 years (top to bottom panels, respectively). The logarithmic greyscale, in units of g cm^{-3}, is given by the vertical bar on the right of the bottom panel. The scale in both axes is given in units of 10^{17} cm.

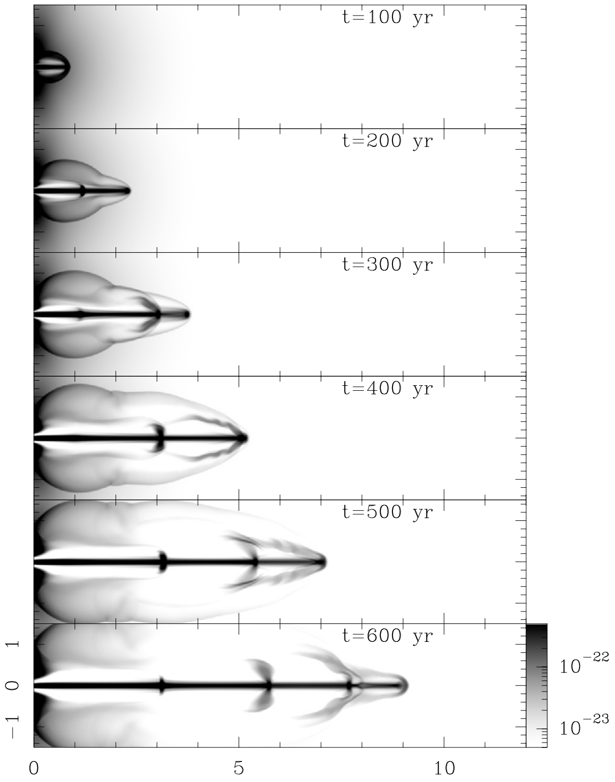

Fig. 3. Same as Fig. 2 but for the case of a jet expanding into an AGB remnant with a density distribution given by Eq. (2) (see text).

4. Results

4.1. Temporal evolution of jet structure for 2D numerical simulations

Figure 2 shows a 600 yr time-sequence of the density stratification (in the rz-plane) for the case of a jet moving into a homogeneous environment. Figure 3 shows a similar time-sequence, but for a jet propagating into the AGB wind (with a density distribution given by Eq. (2)).

The gray-scale representations of the density stratifications obtained for integration times from 100 to 600 years (see Figs. 2 and 3) show the head of the jet traveling away from the injection point. The ejection velocity time variability produces internal working surfaces that travel down the jet (which we identify with the emitting knots of the observed jet). Each working surface is produced when fast material catches up with slower material ejected at earlier times.

The temporal variability law used for the velocity in these simulations corresponds to the superposition of two terms: a periodic variability (described by a sinusoidal function) and a linear increase in the velocity. While a linearly increasing ejection velocity vs. time produces a single, accelerating leading working surface (see Raga et al. 1990 and Cantó et al. 2000), the sinusoidal mode (which is superimposed on the linear ejection velocity vs. time dependence, see Eq. (1)) produces a train of internal working surfaces which travel down the jet beam (see, e.g., Raga & Noriega-Crespo 1998).

A comparison between Figs. 2 and 3 illustrates the effect of the stratified environment on the evolution of the knots. Initially (at times <300 yr), the head of the jet propagates faster in the uniform environment model. However, as the time-evolution proceeds, the head of the jet in the AGB wind case accelerates as it gets out to the lower density regions farther away from the source, and the jet eventually becomes longer than the one of the homogeneous environment jet model (see the t = 600 yr model of Figs. 2 and 3).

An interesting difference between the homogeneous environment and the AGB wind models can be seen in the Hα emission maps (Fig. 4). While the uniform environment jet model shows extended bow shock wings (associated with the leading working surface), the AGB wind model does not show such wings. This is a direct result of the fact that at distances of $\sim 10^{18}$ cm from the source the AGB wind has a very low density, so that the emission from the bow shock is much lower than in the homogeneous environment model.

In this way, we see that the model of a jet travelling into an AGB wind produces Hα intensity maps that more closely resemble the observations of the Hen 3-1475 jet, as this object does not show emission from extended bow shock wings associated with the jet head. Because of this, we carry out 3D simulations only for the case of a jet moving into an AGB wind, and do not study 3D models of jets moving into a uniform environment.

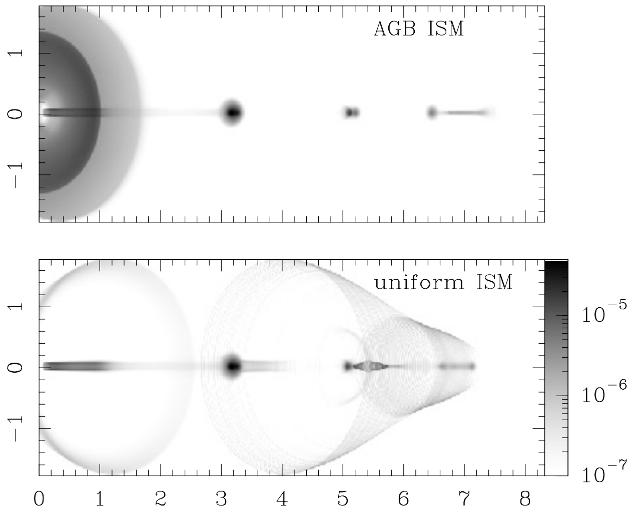

Fig. 4. Comparison between simulated Hα emission for a model with a jet propagating into an uniform ISM (*bottom panel*), and the corresponding emission for the case of a jet moving into an AGB wind (*top panel*). Both maps have been obtained integrating the Hα emission coefficient along lines of sight, for an angle of 50° between the flow axis and the plane of the sky. Both maps correspond to a time-integration of 640 yr. The horizontal and vertical axes are given in arcseconds (for a distance of 5.8 kpc to the object). The Hα emission is depicted with a logarithmic scale (in units of erg s^{-1} cm^{-2} sr^{-1}) given by the vertical bar on the right of the bottom panel.

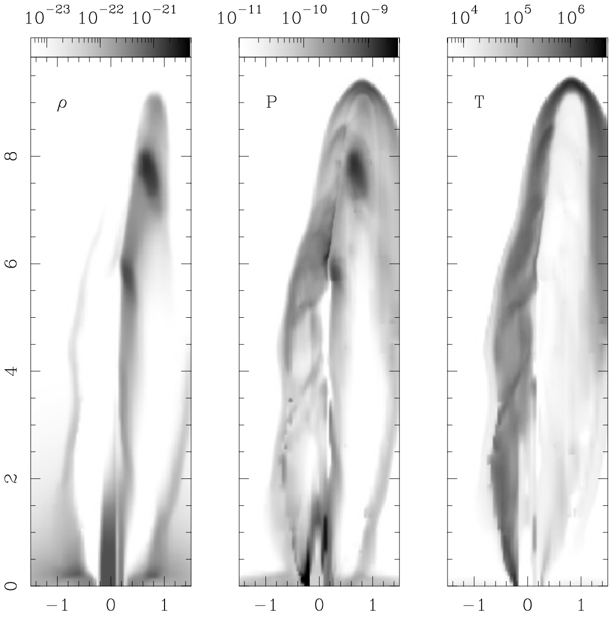

Fig. 5. Density (*left*), pressure (*centre*) and temperature (*right*) stratifications for a precessing jet moving into an AGB wind, obtained from the 3D numerical simulation described in the text. Each panel shows a cut (on the $y-z$ plane) of the corresponding variable for a 640 yr integration time. The scales of both axes are in units of 10^{17} cm. The density, pressure and temperature scales are logarithmic (top horizontal bar on each panel), given in g cm^{-3} dyn cm^{-2} and K, respectively.

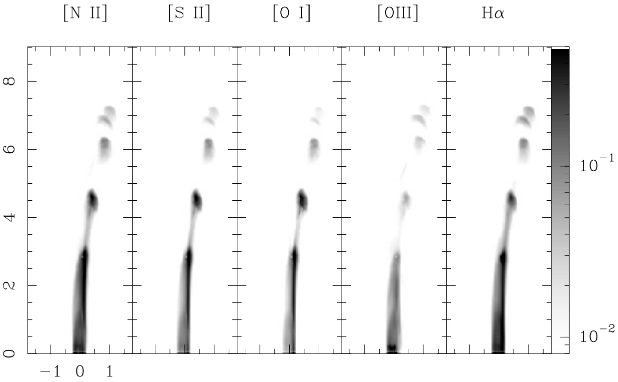

Fig. 6. [N II] 6583 Å, [S II] (6717+6730) Å, [O I] 6300 Å, [O III] 5007 Å and Hα emission maps (from left to right), corresponding to an integration time of 640 yr. These maps have been obtained integrating the emission line coefficient along of lines of sight, considering that the jet axis has an angle of 50° respect to the plane of the sky. The horizontal and vertical axis are in arcseconds (after considering a distance of 5.8 kpc) while the vertical bar on the right, shows (in logarithmic scale) the normalized emission.

4.2. Comparison between 3D numerical results and HST observations

Figure 5 shows cuts on the $y-z$ plane of the density (left), pressure (centre) and temperature (right) stratifications, for the 3D simulation of a precessing jet moving into an AGB wind (see Sect. 3.2). These stratifications correspond to an integration time of 640 yr.

From the density stratification (left panel of Fig. 5), we see that the jet has a leading head, followed by two high density knots, which coincide with high-pressure regions (central panel). There is a high-temperature ($>10^6$ K) region which corresponds to the "cocoon", while the internal jet regions have temperatures $\sim 10^5$ K or lower (right hand panel of Fig. 5).

The main effect of the precession is to produce a curved morphology for the jet beam, which qualitatively resembles the "S"-shaped morphology of the Hen 3-1475 jet (see Fig. 5). Otherwise, the 3D model has internal working surfaces which are similar to ones of the axisymmetric models (see Sect. 4.1).

The predictions obtained from the 3D model can be compared with the WFPC2 HST images and with the position-velocity diagrams obtained from the (spatial and spectral) high-resolution STIS spectroscopy. In order to compare the 3D numerical simulation with the HST images of Hen 3-1475, from the model we have computed intensity maps for the Hα, [N II] 6583 Å, [O I] 6300 Å, [S II] (6717+6731) Å and [O III] 5007 Å (from left to right, Fig. 6) integrating the emission coefficient along lines of sight. We have assumed that the y-axis lies in the plane of the sky, and that the z-axis is oriented toward the observer at an angle of 50° with respect to the plane of the sky. Furthermore, we have changed the physical coordinates of the model to angular sizes (after taking into account distance and projection effects).

In Fig. 6, we show the simulated line emission maps for a 640 yr integration-time, which can be compared with the HST [N II] image of the SE jet (shown in Fig. 7). The images of Hen 3-1475 obtained with the HST using narrow band filters (such as $F658N$) essentially trace the ionized gas through the detection of the nebular emission coming from the corresponding emission line (such as [N II] 6583 Å). However, we should

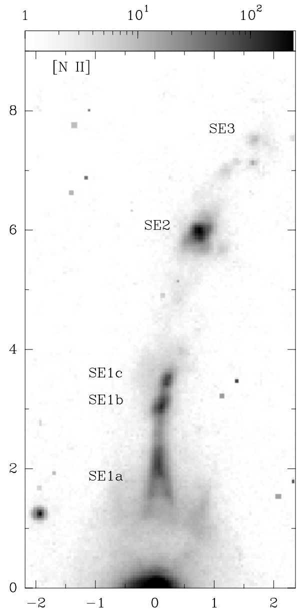

Fig. 7. HST image in [N II] of Southeastern outflow of Hen 3-1475, which exhibits a jet-like structure and three pairs of symmetric emission knots. The innermost pair of knots show subarcsecond structure, with the existence of three well defined compact subcondensations. The knots have been labeled following Riera et al. (2003).

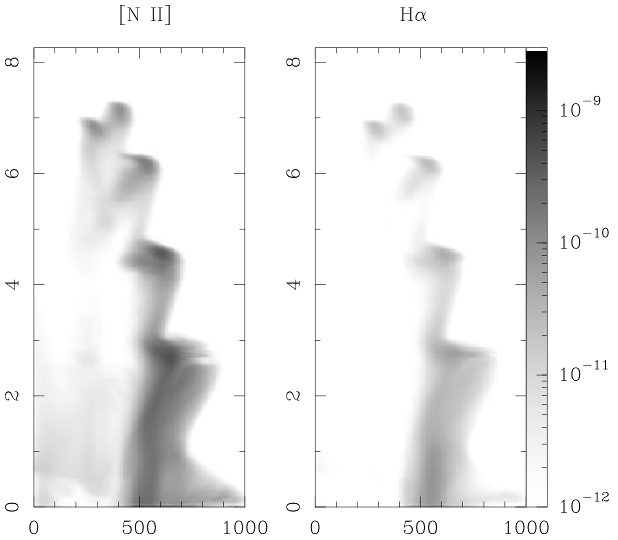

Fig. 8. PV diagram for emission in [NII] (*left panel*) and Hα (*right panel*), for an integration time of 640 yr. An angle of 50° between the plane of the sky and the jet direction has been considered. The horizontal axis is given in units of km s^{-1} while the vertical axis is in arcseconds. The [NII] and Hα emission are shown in logarithmic scale by the bar on the right, in units of erg s^{-1} cm^{-2} sr^{-1}.

note that losses are expected in the detection of the extremely blueshifted and redshifted emission due to the large velocities involved. Therefore, the observed intensities of the knots in the [N II] image are underestimated due to the reduced transmission of the filter $F658N$. The losses are larger for the innermost knots, which show the largest radial velocities.

All of the maps (from high to low-ionisation species) show the same number of knots (at the same distances from the injection point) with similar morphologies. Comparing the observed [N II] image (Fig. 7) with the simulated emission line maps (Fig. 6), it is clear that the observed and simulated maps are qualitatively similar.

At t = 640 yr (see Fig. 6), we see the leading head at an angular distance of $\sim 7\farcs3$ from the injection point, which agrees well with the observed angular distance of $7\farcs57$ from the central source to the outermost knot SE3. In all of the simulated emission line maps we observe that the leading head has a double structure. Actually, this double feature corresponds to two working surfaces. This pair of knots is formed by a faster working surface which at t = 640 yr has just overtaken a slower working surface ejected earlier (this dynamical effect can be seen in the PV diagrams of Fig. 8).

The intermediate knot (labeled SE2 in Fig. 7) is located at a distance of $\sim 5\farcs9$ in both the observed and simulated images. The observed innermost knot (labeled SE1a, SE1b and SE1c) is an elongated structure formed by three subcondensations (at distances from the source from $\sim 2\farcs27$ to $3\farcs65$). No emission is observed in the innermost region (i.e. between SE1a and the central source). In the inner region, the simulated maps (see Fig. 6) show an elongated feature connecting the point of injection with a compact knot at $\sim 4\farcs5$ down the jet. This feature clearly resembles the morphology observed in the innermost knot (SE1) of the Hen 3-1475 jet. However, the calculated emission maps do not show the observed emission gap between this knot and the source.

A detailed comparison of the intensity maps of low-ionization (i.e. [O I] or [S II]) and high-ionization species (i.e. [O III]), reveals that the leading bow-shock is prominent in [O III] and Hα, and much fainter than the other knots in the low-ionization species (see, e.g., the [O I] intensity map of Fig. 6). The simulated [O I] intensity map shows a large range of intensities from the bright innermost knot to the fainter leading head. All knots show a more or less constant [O III] intensity (from the inner knots to the head). Unfortunately, no spectrophotometric observations of the three knots of Hen 3-1475 (covering the wavelength range from 5000 to 6800 Å) have been published.

Figure 8 displays position–velocity (PV) diagrams in [NII] 6583 Å (left) and Hα (right), obtained from our simulations for an integration time of 640 yr. Both maps have been convolved with a spectral resolution of 50 km s^{-1}, in order to simulate the STIS spectral resolution. In order to have predictions that can be directly compared with the spectroscopic observations (Borkowski & Harrington 2001; Riera et al. 2003; Riera 2004), the line profiles have been computed assuming a broad spectrograph slit (covering all of the computational domain along the y-axis) straddling the z-axis. Again, an angle of 50° between the z-axis and the plane of the sky has been assumed.

The calculated PV diagrams (see Fig. 8) qualitatively reproduce several characteristics of the observed kinematics. As expected, the large radial velocities and the observed decrease of the radial velocity with distance along the Hen 3-1475 jet are well reproduced by the model. Also, the models show distinctive step-like radial velocity decreases along the jet axis, and such an effect is also seen in the observed PV diagrams (see Fig. 8 and Riera 2004).

The observed emission line profiles arising from the knots show wide double-peaked profiles (Borkowski & Harrington 2001; Riera et al. 2003). In the innermost knots the high-velocity peak is stronger than the low-velocity peak, while the situation reverses at the intermediate knots. The calculated PV diagrams show broad emission line profiles, but which are narrower than the observed profiles by a factor of ∼2. Also, the calculated PV maps show double-peaked profiles only at very specific spatial locations (e.g., in the knot at ≈4.″7 from the source in Fig. 8).

5. Discussion and conclusions

We have carried out 2D (axisymmetric) and 3D numerical simulations for modeling the jet of the proto-planetary nebula Hen 3-1475, which is the first attempt for obtaining a full and dynamical model for the outflows associated with this nebula.

We have found that it is possible to fit the observed structure of the Hen 3-1475 jet with a time-dependent jet model with an ejection velocity history composed of a sinusoidal mode superimposed on a linear ramp (i.e., a linear increase of the ejection velocity with time). The sinusoidal mode has a period of ∼120 years and a half-amplitude of 150 km s^{-1}, and the linear term has a slope of 1 km s^{-1} yr^{-1}. We have explored models of jets moving into a homogeneous environment, as well as models of jets moving into a previously ejected, stratified AGB wind.

We should note that Lee & Sahai (2003) have presented 2D hydrodynamical simulations of the interaction of a CFW/jet and a spherical AGB wind in a PPN. Lee & Sahai adopted a periodic variation in the density and velocity of the jet (with an amplitude of 150 km s^{-1} and a period of 22 yr, keeping a constant mass loss rate) in order to reproduce the morphology and velocities observed in the PPN CRL 618. A model including both periodic density and ejection velocity variations could describe the characteristics of PPNs such as Hen 3-1475. However, Lee & Sahai (2003) point out some difficulties for producing the knotty structure observed along the axis of PPN CRL 618. It is unclear whether or not this kind of velocity and density variability would work well for modelling the knot structure of the PPN Hen 3-1475.

From the numerical models we have obtained simulated [NII], [SII], [OI], [OIII] and Hα maps, as well as PV diagrams, which can be directly compared with the observational results which have been previously obtained with the HST. A comparison between the simulated emission maps (obtained from the 2D and 3D numerical simulations) and the observations shows that a model of a variable speed precessing jet (with a period of 1500 yr and the ejection velocity history discussed above) moving into a previously ejected AGB wind produces the best agreement (of all of the computed models) with the observed characteristics of the Hen 3-1475 jet.

The observed string of shock-excited knots is well reproduced in our simulated maps. Also, the knot positions are similar to the observed ones, and are distributed along a curved locus which resembles the S-like shape observed in HST images of the Hen 3-1475 jet (see Figs. 6 and 7).

With respect to the kinematical characteristics, by comparing the calculated and the observed PV diagrams we can say that our model succesfully explains:

- the large observed radial velocities;
- the decrease of the radial velocity of the knots with increasing distances from the source;
- step-like changes in radial velocity at the positions of the knots;
- the existence of broad emission line profiles.

However, the simulated profiles from 3D simulations are narrower than the observed ones (by a factor of 2), and do not show double-peaked profiles with strong emission at the highest velocities.

From this discussion, we conclude that many of the morphological and kinematical features of the Hen 3-1475 jet can indeed be reproduced (at least in a qualitative way) by a model of a variable ejection velocity, precessing jet. This quite promising result gives a framework for modelling and interpreting future, more detailed observations of this jet, which could lead to more stringent constraints for the proposed model. Finally, if taken seriously, the parameters of our model give an idea of what are the variability periods and amplitudes (as well as the precession) associated with the ejection from Hen 3-1475, which in principle provide constraints on the nature of the stellar source.

Acknowledgements. Authors thank Saul Rappaport (the referee) for his useful suggestions which help us to improving the previous version of this manuscript. A.C.R. and P.F.V. acknowledge financial support from Conacyt (Mexico) grants 36572-E and 41320-E, and DGAPA (UNAM) grant IN 112602. The work of ARi was supported by the MCyT grant AYA2002-00205 (Spain). We also acknowledge Israel Díaz for maintaining and supporting our multiprocessor Linux server, where we have carried out our numerical simulations, and Antonio Ramírez for computer help.

References

Blackman, E. G., Frank, A., & Welch, C. 2001, ApJ, 546, 288
Bobrowsky, M., Zijlstra, A. A., Grebel, E. K., et al. 1995, ApJ, 446, L89
Borkowski, K. J., Blondin, J. M., & Harrington, J. P. 1997, ApJ, 482, L97
Borkowski, K. J., & Harrington, J. P. 2001, ApJ, 550, 778
Bujarrabal, V., Castro-Carrizo, A., Alcolea, J., & Sánchez Contreras, C. 2001, A&A, 377, 868
Cantó, J., Raga, A. C., & D'Alessio, P. 2000, MNRAS, 313, 656
García-Arredondo, F., & Frank, A. 2004, ApJ, 600, 992
García-Lario, P., Manchado, A., Pych, W., & Pottasch, S. R. 1997, A&AS, 126, 479
García-Lario, P., Riera, A., & Manchado, A. 1999, ApJ, 526, 854
García-Segura, G., Langer, N., Rózyczka, M., & Franco, J. 1999, ApJ, 517, 767
García-Segura, G., & López, J. A. 2000, ApJ, 544, 336
Guerrero, M. A., Chu, Y. H., & Gruendl, R. A. 2004, Asymmetric Planetary Nebulae III, ASP Conf. Ser., in press

Huggins, P. J., Muthu, C., Bachiller, R., Forveille, T., & Cox, P. 2004, A&A, in press

Kingsburgh, R. L., & Barlow, M. J. 1994, MNRAS, 271, 257

Knapp, G. R., Bowers, P. F., Young, K., & Phillips, T. G. 1995, ApJ, 455, 293

Lee, C.-F., & Sahai, R. 2003, ApJ, 586, 319

Masciadri, E., Velázquez, P. F., Raga, A. C., Cantó, J., & Noriega-Crespo, A. 2002, ApJ, 573, 260

Mellema, G. 1995, MNRAS, 277, 173

Raga, A. C., Cantó, J., Binette, L., & Calvet, N. 1990, ApJ, 364, 601

Raga, A. C., & Noriega-Crespo, A. 1998, AJ, 116, 2952

Raga, A. C., Navarro-González, R., & Villagran-Muniz, M. 2000, RMxAA, 36, 67

Raga, A. C., Velázquez, P. F., Cantó, J., & Masciadri, E. 2002, A&A, 395, 647

Riera, A., García-Lario, P., Manchado, A., Pottasch, S. R., & Raga, A. C. 1995, A&A, 302, 137

Riera, A., García-Lario, P., Manchado, A., Bobrowsky, M., & Estalella, R. 2002, RMxAA (Serie de Conferencias), 13, 127

Riera, A., García-Lario, P., Manchado, A., Bobrowsky, M., & Estalella, R. 2003, A&A, 401, 1039

Riera, A. 2004, Asymmetric Planetary Nebulae III, ASP Conf. Ser., in press

Rodrigues, C. V., Jablonski, F. J., Gregorio-Hetem, J., Hickel, G. R., & Sartori, M. J. 2003, ApJ, 587, 312

Sahai, R., & Trauger, J. T. 1998, AJ, 116, 1357

Sahai, R., Kastner, J. H., Frank, A., Morris, M., & Blackman, E. G. 2004, ApJL, in press

Sánchez Contreras, C., & Sahai, R. 2001, ApJ, 533, L173

Soker, N., & Livio, M. 1994, ApJ, 421, 219

Soker, N., & Rappaport, S. 2000, ApJ, 538, 241

Trammell, S. R., & Goodrich, R. W. 2002, ApJ, 579, 688

Ueta, T., Meixner, M., & Bobrowsky, M. 2000, ApJ, 528, 861

van Leer, B. 1982, ICASE Report, No., 82-30

Völker, R., Smith, M. D., Suttner, G., & Yorke, H. W. 1999, A&A, 343, 953

Ziljstra, A. A., Chapman, J. M., te Lintel Hekkert, P., et al. 2001, MNRAS, 322, 280